

CSV-ViT: A Vision Transformer with the Variable-sized Cortical Supervertices for Detection of Alzheimer’s Disease Pathologies

Geonwoo Baek¹[0009–0001–2338–4575] and Ikbeom Jang^{1*}[0000–0002–6901–983X]

Department of Computer Science and Engineering,
Hankuk University of Foreign Studies, Seoul, Republic of Korea
{phlox3959, ijang}@hufs.ac.kr

Abstract. Confirming Alzheimer’s disease (AD) typically relies on positron emission tomography (PET), which remains costly and invasive, motivating the use of structural MRI-based prescreening. Deep learning on non-Euclidean manifolds, particularly brain cortical surfaces, faces significant challenges due to the data’s spherical topology. Recent surface models have enabled learning from cortical surface data; however, imposing face-based uniform patches often causes duplicate vertices at patch boundaries. In general, many surface-based models are limited in their awareness of the region of interest (ROI), which can result in non-cortical regions, such as the medial wall, being included. We propose a cortical surface tokenization that performs ROI-preserving, vertex-based, variable-sized patch partitioning. We refer to these cortical surface patches as cortical supervertices (CSVs). Building on this representation, we design the CSV Vision Transformer (CSV-ViT), a variable-size patch-tolerant Vision Transformer that uses padding and a mask-aware patch embedding. We used T1-weighted MRI and evaluated our framework by classifying AD-related status into three categories: AD diagnosis, amyloid positivity, and tau positivity. Across the experiments, CSV-ViT achieved higher classification performance than recent surface-based models. The results suggest that the proposed CSV-ViT may support MRI-based prediction of AD-related status prior to PET or CSF confirmation.

Keywords: Cortical Surface Analysis · Vision Transformers · Alzheimer’s Disease · 3D Mesh Encoder · Morphometric Analysis

1 Introduction

Self-attention enables transformers to model long-range dependencies, but applying attention at the pixel level is computationally prohibitive. Vision Transformer (ViT) addresses this by partitioning an image into patches and applying attention to patch tokens [8], offering a practical trade-off between representational capacity and computational burden.

* Corresponding author.

Alzheimer’s disease (AD) is characterized by neuropathology that accumulates over time, and confirmation often relies on β -amyloid ($A\beta$) and tau biomarkers measured by positron emission tomography (PET) or in cerebrospinal fluid (CSF). However, PET and CSF are limited in accessibility due to cost and invasiveness. MRI-based prediction of PET/CSF-derived pathology can support prescreening before the tests. This motivates surface-based learning on template-registered meshes, in which corresponding cortical locations align across subjects, as explored by recent models such as the Surface Vision Transformer (SiT) [1]. In this study, we perform three binary classifications: diagnosis (Dx) and PET-derived $A\beta$ and tau status, using cortical thickness (CT) and curvature (Curv) as inputs.

However, importing the fixed-size patch assumption to cortical meshes is non-trivial. Because cortical regions of interest (ROIs) vary substantially in size and geometry, uniform patching can result in patches spanning multiple ROIs, thereby mixing ROIs and weakening region-specific representations. In addition, mesh patching can introduce unwanted artifacts: face-based partitioning may duplicate boundary vertices across patches, and template registration may include non-cortical areas, such as the medial wall, unless explicitly handled.

To address these issues, we propose an ROI-preserving cortical surface partitioning that produces non-overlapping patches without ROI mixing. The resulting cortical supervertices (CSVs) naturally vary in size across ROIs. We then design CSV-ViT, a surface ViT that supports variable-sized CSV patches via padding and a mask-aware patch embedding. By enabling attention over ROI-pure, non-overlapping patches, our framework balances attention granularity and computational burden, thereby improving the modeling of cortical features for Dx, $A\beta$, and tau.

Existing methods. Prior learning methods for cortical surfaces include graph-based models such as DiffusionNet [2] and SurfGNN [4], and transformer-based approaches such as the Surface Vision Transformer (SiT) [1] and the Multiscale Surface Vision Transformer (MS-SiT) [3]. SiT-style models enable long-range interactions via patch tokens on registered meshes, but their fixed-size tokenization can induce ROI mixing. In contrast, we focus on surface tokenization and couple ROI-preserving, non-overlapping partitioning with a variable-size-aware transformer input interface.

Contribution. We propose an ROI-preserving cortical partition that avoids ROI mixing while ensuring non-overlapping vertices, and introduce CSV-ViT, a mask-aware embedding that ingests variable-sized CSV patches. This is a proof-of-concept demonstrating the use of variable-sized patches in ViTs for learning from cortical surface features. On classification of Dx, $A\beta$, and tau on a multi-cohort dataset, we show consistent improvements over recent surface baselines and validate the impact of each component via targeted ablations.

2 Methods

Fig. 1 illustrates the overall framework, from cortical surface partitioning to classification using CSV-ViT.

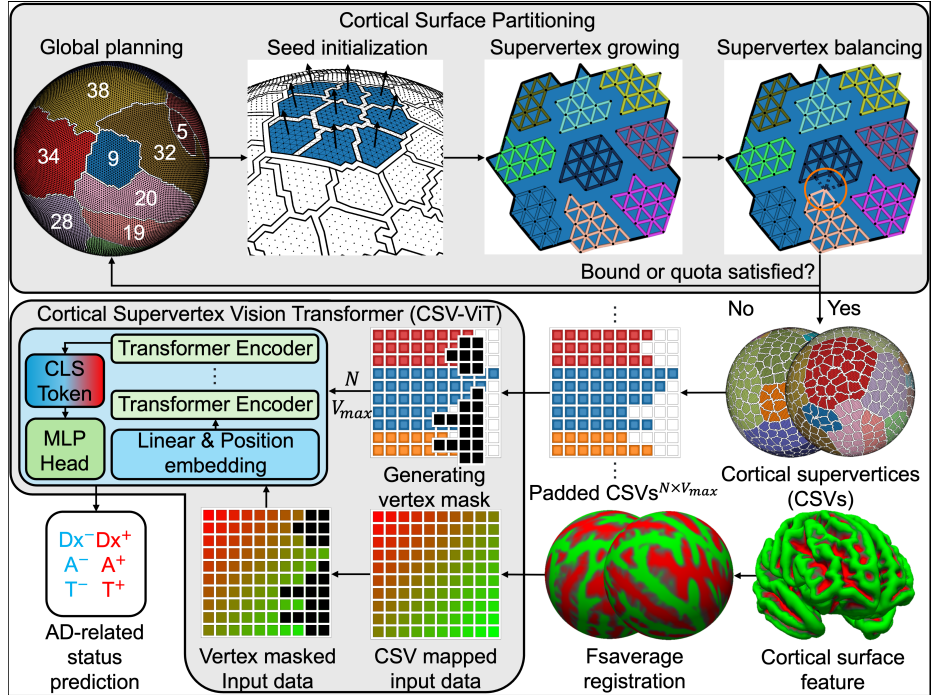


Fig. 1. Overview of the proposed framework, including cortical surface partitioning and the CSV-ViT.

Partitioning for CSV-ViT. We register FreeSurfer cortical surfaces to fsaverage6 (ico6; 40,962 vertices per hemisphere) and partition each hemisphere into ROI-constrained cortical supervertices (CSVs) using the Desikan–Killiany atlas. To mitigate ROI mixing caused by atlas artifacts, minor disconnected fragments (<10% of an ROI) are reassigned to the adjacent ROI with the largest boundary contact; non-cortical labels (e.g., the medial wall) are excluded. We model the ico6 mesh as a graph $G = (V, E)$ with 1-ring adjacency and construct connected CSVs within each ROI under a global size bound $L \leq |SV| \leq H$. The procedure comprises four stages: global planning, seed initialization, supervortex growth, and supervortex balancing, with fallback loops when constraints are not met.

Global planning. Given a target CSV count per hemisphere K_{total} , we search for a feasible bound (L, H) and ROI-wise counts $\{K_r\}$ such that $\sum_r K_r = K_{\text{total}}$

and each ROI r (with n_r vertices) satisfies:

$$\left\lceil \frac{n_r}{H} \right\rceil \leq K_r \leq \left\lfloor \frac{n_r}{L} \right\rfloor. \quad (1)$$

Among feasible allocations, we select $\{K_r\}$ to reduce ROI-wise imbalance by minimizing $\sum_r (n_r/K_r - \bar{s})^2$, where $\bar{s} = (\sum_r n_r)/K_{\text{total}}$. We try candidates from tighter to looser bounds and proceed only if later stages succeed.

Seed initialization. For each ROI, we handle multiple connected components by distributing K_r among them as needed. We initialize K_r seeds via farthest-point sampling (FPS) on vertex direction vectors, and optionally refine the seeds using METIS [9] to obtain balanced subgraphs (falling back to FPS if METIS fails).

Supervortex growing. Within each ROI component, we define near-equal integer quotas (size difference ≤ 1) and grow SVs by absorbing unassigned 1-ring boundary vertices, which preserves connectivity. SVs with lower quota fill ratios are expanded first. If any SV fails to meet its quota after growing, we update seeds based on the current assignment and repeat the seed-grow step up to a fixed number of retries.

Supervortex balancing. We then enforce the bound $L \leq |SV| \leq H$ by transferring boundary vertices between adjacent SVs on an SV adjacency graph while preserving connectivity. If any SV still violates the bound after balancing, we reject the current plan and return to **global planning** to retry with a looser $(L, H, \{K_r\})$.

Finally, we obtain 642 ROI-preserving CSVs per hemisphere (cortex-only, lossless, non-overlapping). Each CSV is represented by its vertex-index list and padded with -1 to the maximum CSV size ($V_{\text{max}} = 69$) for model input.

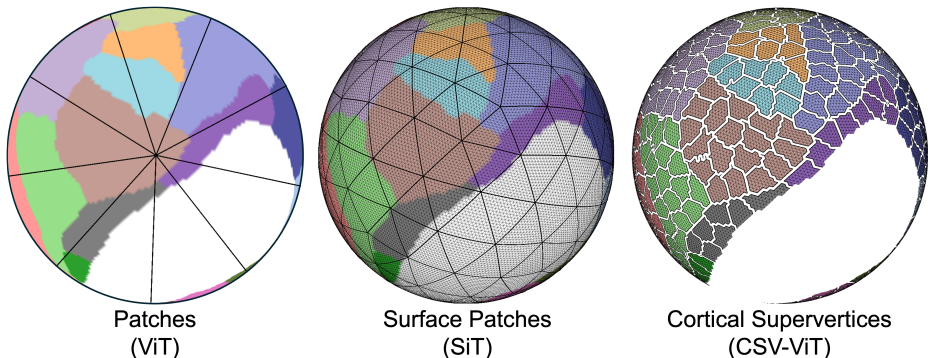


Fig. 2. Difference of Patch across ViT, SiT, and CSV-ViT

2.1 Cortical Supervertex Vision Transformer

CSV-ViT represents a subject by variable-sized CSVs. Fig. 2 shows the differences in patch tokenization among ViT, SiT, and CSV-ViT. Given per-vertex cortical features on the ico6 mesh with C channels and a precomputed CSV map, we collect the vertices of each CSV and pad them to a fixed maximum length V_{\max} . This yields an input tensor $\mathbf{X} \in \mathbb{R}^{B \times C \times N \times V_{\max}}$, where N is the number of CSVs (both hemispheres). We build a binary mask $\mathbf{M} \in \{0, 1\}^{N \times V_{\max}}$ from the CSV map and zero-out padded entries before embedding.

Mask-aware patch embedding. We flatten the vertices within each CSV and apply a single linear layer to obtain a single token per CSV. After masking, each CSV token is computed as:

$$\mathbf{t}_i = \text{Linear}(\text{vec}(\mathbf{x}_i)), \quad i = 1, \dots, N, \tag{2}$$

where $\mathbf{x}_i \in \mathbb{R}^{C \times V_{\max}}$ is the padded CSV feature matrix, and $\text{vec}(\cdot)$ concatenates the vertex and channel dimensions.

2.2 Classification for Alzheimer’s disease-related pathology

We performed three binary classifications of Dx, A, and T status to evaluate the proposed framework on a multi-cohort dataset. In addition to two cortical surface features, including CT and Curv, we provided CSV-ViT with the CSV partition map, which defines $N = 1284$ CSVs (both hemispheres) and a maximum CSV size of $V_{\max}=69$.

3 Results and Discussion

3.1 Experimental Setting

To assess our framework, we formulated three binary classification problems: Dx, $A\beta$ positivity, and tau positivity. To reduce diagnostic label heterogeneity when integrating ADNI and OASIS, we restricted all tasks to participants labeled as AD or CN in both cohorts and excluded mild cognitive impairment (MCI); MCI is clinically/biologically heterogeneous and its operational definition (including the boundary with very mild dementia) can vary across studies and cohorts [10,11,12,13,14]. We standardized all three problems as binary classification so that the model solves the same kind of tasks. Because tau pathology is often more tightly coupled with neurodegeneration than $A\beta$ [15,16,17], tau positivity is frequently expected to be more predictable from structural MRI-derived morphometry. Nevertheless, MRI-based biomarker prediction performance depends on cohort composition, label definitions, and prevalence, and amyloid prediction can match or exceed tau prediction; for example, Lew *et al.* reported higher AUROC for predicting PET-determined $A\beta$ status than tau status using MRI volumes and readily available clinical variables [18].

We report the area under the receiver operating characteristic curve (AUROC) as the primary metric and balanced accuracy (Bacc) as a secondary metric

across all experiments. We compared our method against the latest surface-based models, including SiT [1], DiffusionNet [2], MS-SiT [3], and SurfGNN [4].

We used 4-fold cross-validation with a fixed fold assignment so that all models were trained and tested on identical splits. For each fold, three folds were used for training, and one for testing; a validation set was created by holding out 10% of the training data with stratification. To address class imbalance, we optimized a class-weighted binary cross-entropy (BCE) loss, where the positive class weight was set to the ratio of negative-to-positive samples computed on the training split of each fold. Unless otherwise stated, we report mean \pm standard deviation (std) across folds.

3.2 Data and Preprocessing

We used public data from the Alzheimer’s disease neuroimaging initiative (ADNI)¹ and the Open Access Series of Imaging Studies (OASIS)². In ADNI, we included accelerated scans to maximize the number of participants. In OASIS, only fully-sampled scans were available. To assess generalizable performance, we combined these two cohorts despite differences in MRI protocols. Information on participants is presented in Table 3.2. We used T1-weighted (T1w) MR images to extract cortical features. For each subject, the first accessible data were used if there were multiple sessions, and each participant contributed only once. Because not all subjects had a matched PET scan, the participant counts differ across the Dx, A β , and tau classifications. A β and tau labels were derived from PET (AV45 [6] for A β and AV1451 [7] for tau), and positivity cutoffs were set according to the cohort documentation. For Dx, we considered an AD vs. CN classification setting.

All T1w MR images were processed with FreeSurfer v7.4.1 [5] to reconstruct cortical surfaces and extract vertex-wise CT and Curv. Only data that passed FreeSurfer quality control were retained. The data were then registered to the fsaverage template, represented as an icosahedral subdivision level 6 (40,962 vertices per hemisphere), and left/right hemispheres were concatenated.

Table 1. Participants’ statistics of the datasets in this study. For A and T, labels indicate PET-based positivity (positive vs. negative); for N (neurodegeneration), labels indicate AD vs. cognitively normal (CN). The values are number of subjects (n), target prevalence (%P), ratio of females (%F), and age (mean \pm std (min–max)). Only available participants were reported. No subject was included more than once.

| Target | Cohort | n | %P | CN | AD | %F | Age |
|-----------|--------|------|------|------|-----|------|----------------------------|
| Diagnosis | ADNI/ | 1451 | 25.5 | 1081 | 370 | 57.3 | 71.4 \pm 9.1 (45.8–97.1) |
| Amyloid | OASIS | 409 | 49.4 | 314 | 95 | 56.7 | 73.5 \pm 8.4 (55.3–92.5) |
| Tau | | 536 | 20.9 | 490 | 46 | 63.6 | 70.0 \pm 9.2 (46.0–96.1) |

¹ <https://adni.loni.usc.edu>

² <https://www.oasis-brains.org>

3.3 Classification Performance

CSV-ViT against latest surface models.

Table 3.3 summarizes the classification performance of surface-based baselines (SiT, DiffusionNet, MS-SiT, and SurfGNN) and our CSV-ViT on Dx, Aβ, and tau using CT and Curv as inputs. Overall, CSV-ViT achieves higher classification performance than the latest surface-based models.

Among the five models, DiffusionNet and SurfGNN are ROI-agnostic and do not enforce any ROI constraints, whereas SiT and MS-SiT may exhibit ROI mixing because their patches may span multiple ROIs. Therefore, CSV-ViT is the only method that preserves ROI boundaries at the input level; by CSV partitioning, it also keeps vertices disjoint and excludes non-cortical vertices (e.g., medial wall). Since CSV-ViT consistently outperforms SiT and MS-SiT across all tasks, we infer that using cortex-only vertices, preventing vertex duplication, and preserving ROIs at the tokenization stage contribute meaningfully to improved classification performance.

We observe that CT generally provides stronger predictive signals than Curv for Dx, Aβ, and tau, except for SiT on tau, where the two features perform similarly. Notably, CSV-ViT improves performance across both feature sets, indicating that adopting the proposed variable-sized patches in a ViT is effective for learning from cortical surface features.

Table 2. Classification results of surface-based models. The inputs are CT and Curv. We report mean±std. We highlight the **best** and second test results. * $p < 0.05$; ** $p < 0.01$.

| Model | Target | Cortical thickness | | Cortical curvature | |
|------------------|--------|----------------------|--------------------|--------------------|-----------------------|
| | | AUROC | Bacc | AUROC | Bacc |
| SiT [1] | Dx | 0.809±0.028** | 0.732±0.032* | 0.696±0.055** | 0.629±0.044** |
| DiffusionNet [2] | | 0.821±0.047** | 0.738±0.038 | 0.558±0.034** | 0.520±0.016** |
| MS-SiT [3] | | 0.851±0.024 | 0.773±0.032 | 0.723±0.065** | 0.658±0.053 |
| SurfGNN [4] | | 0.758±0.030** | 0.698±0.022** | 0.527±0.128** | 0.524±0.046** |
| CSV-ViT (ours) | | 0.852±0.014 | <u>0.764±0.025</u> | 0.755±0.035 | 0.674±0.043 |
| SiT [1] | Aβ | 0.644±0.048** | 0.569±0.036** | 0.522±0.027 | 0.502±0.018 |
| DiffusionNet [2] | | <u>0.705±0.051</u> * | 0.581±0.062* | 0.534±0.054 | 0.516±0.020 |
| MS-SiT [3] | | 0.689±0.034** | <u>0.645±0.030</u> | <u>0.559±0.059</u> | <u>0.528±0.037</u> |
| SurfGNN [4] | | 0.687±0.051** | 0.573±0.032** | 0.543±0.048 | 0.519±0.040 |
| CSV-ViT (ours) | | 0.729±0.061 | 0.668±0.058 | 0.586±0.028 | 0.544±0.035 |
| SiT [1] | Tau | 0.516±0.031** | 0.502±0.011 | 0.518±0.037 | 0.505±0.031* |
| DiffusionNet [2] | | 0.572±0.064 | 0.554±0.047 | 0.534±0.014 | <u>0.549±0.016</u> ** |
| MS-SiT [3] | | <u>0.596±0.026</u> | <u>0.556±0.010</u> | <u>0.536±0.043</u> | <u>0.539±0.014</u> * |
| SurfGNN [4] | | 0.576±0.070* | 0.546±0.053 | 0.530±0.034 | 0.527±0.021* |
| CSV-ViT (ours) | | 0.611±0.044 | 0.559±0.017 | 0.604±0.032 | 0.584±0.041 |

Table 3. Incremental ablation study of CSV-ViT by Dx, $A\beta$, and tau status classification. The inputs are CT and Curv. Our contributions are: preserving ROI of patches (pROI), vertex-based partitioning (Vtx), and variable-sized CSVs (vCSVs). We report mean \pm std, target (Tgt). Baseline denotes SiT.

| Tgt | Contributions | | | Cortical thickness | | Cortical curvature | | |
|----------|---------------|-----|-------|--------------------|-------------------|--------------------|-------------------|-------------------|
| | pROI | Vtx | vCSVs | AUROC | Bacc | AUROC | Bacc | |
| Dx | Ours | • | • | • | 0.852 \pm 0.014 | 0.764 \pm 0.025 | 0.755 \pm 0.035 | 0.674 \pm 0.043 |
| | | • | • | ○ | 0.829 \pm 0.023 | 0.760 \pm 0.020 | 0.732 \pm 0.049 | 0.640 \pm 0.020 |
| | | • | ○ | ○ | 0.819 \pm 0.028 | 0.711 \pm 0.025 | 0.708 \pm 0.036 | 0.640 \pm 0.021 |
| | Baseline | ○ | ○ | ○ | 0.809 \pm 0.028 | 0.732 \pm 0.032 | 0.696 \pm 0.055 | 0.629 \pm 0.044 |
| $A\beta$ | Ours | • | • | • | 0.729 \pm 0.061 | 0.668 \pm 0.058 | 0.586 \pm 0.028 | 0.544 \pm 0.035 |
| | | • | • | ○ | 0.719 \pm 0.044 | 0.656 \pm 0.028 | 0.575 \pm 0.029 | 0.519 \pm 0.044 |
| | | • | ○ | ○ | 0.711 \pm 0.055 | 0.653 \pm 0.048 | 0.558 \pm 0.011 | 0.537 \pm 0.018 |
| | Baseline | ○ | ○ | ○ | 0.610 \pm 0.044 | 0.653 \pm 0.048 | 0.558 \pm 0.028 | 0.537 \pm 0.018 |
| Tau | Ours | • | • | • | 0.611 \pm 0.044 | 0.559 \pm 0.017 | 0.604 \pm 0.032 | 0.584 \pm 0.041 |
| | | • | • | ○ | 0.606 \pm 0.059 | 0.573 \pm 0.040 | 0.544 \pm 0.095 | 0.513 \pm 0.092 |
| | | • | ○ | ○ | 0.599 \pm 0.033 | 0.583 \pm 0.014 | 0.528 \pm 0.078 | 0.496 \pm 0.020 |
| | Baseline | ○ | ○ | ○ | 0.516 \pm 0.031 | 0.502 \pm 0.011 | 0.518 \pm 0.037 | 0.505 \pm 0.031 |

Ablation study.

Table 3 presents an incremental ablation of our framework by removing each component from CSV-ViT: ROI-preserving tokenization (Ret ROI), vertex-based non-overlapping partitioning (Vtx), and variable-sized patches ($\Delta|SV|$) enabled by padding and a mask-aware embedding. Removing all components reduces the method to the SiT baseline.

All three components improve performance. The largest drop is observed when removing Ret ROI, especially for the harder A and T tasks, indicating the importance of ROI-faithful tokenization. This design also facilitates excluding non-cortical vertices (e.g., the medial wall). Excluding variable-sized patches further degrades performance, consistent with vertex under-coverage that can occur when enforcing uniform patch sizes. Lastly, reverting from vertex-based to face-based partitioning reduces performance, likely due to boundary vertex duplication. Therefore, the results suggest the priority order for cortical surface partitioning is ROI preservation, followed by enabling variable-sized patches and vertex-based partitioning.

4 Conclusion

We proposed an ROI-preserving cortical surface partitioning method that generates variable-sized CSV patches and designed CSV-ViT, a Vision Transformer that can ingest such variable-sized patches via padding and a mask-aware embedding. Our patching produces ROI-preserving and non-overlapping CSVs, enabling inter- and intra-regional attention across cortical regions. Experiments

on multi-cohort Dx, $A\beta$, and tau classification exhibit consistent improvements over recent surface-based baselines, supporting the effectiveness of CSV-ViT for cortical surface features. In future work, we will extend the framework to handle higher-resolution cortical surface representations.

References

1. Dahan, S., Fawaz, A., Williams, L.Z., Yang, C., et al.: Surface Vision Transformers: Attention-Based Modelling applied to Cortical Analysis. In: Medical Imaging with Deep Learning (MIDL). pp. 282–303 (2022). <https://doi.org/10.48550/arXiv.2203.16414>
2. Sharp, N., Attaiki, S., Crane, K., et al.: DiffusionNet: Discretization agnostic learning on surfaces. *ACM Trans. Graph.* **41**(3), 27:1–27:16 (2022). <https://doi.org/10.1145/3507905>
3. Dahan, S., Williams, L. Z., et al.: The Multiscale Surface Vision Transformer. arXiv preprint arXiv:2303.11909 (2024). <https://doi.org/10.48550/arXiv.2303.11909>
4. Li, Z., Zhang, J., et al.: SurfGNN: A robust surface-based prediction model with interpretability for coactivation maps of spatial and cortical features. *Medical Image Analysis* **107**, 103793 (2025). <https://doi.org/10.1016/j.media.2025.103793>
5. Fischl, B., Van Der Kouwe, A., et al.: Automatically parcellating the human cerebral cortex. *Cerebral Cortex* **14**(1), 11–22 (2004). <https://doi.org/10.1093/cercor/bhg087>
6. Johnson, K.A., Sperling, R.A., Gidicsin, C.M., Carmasin, J.S., Maye, J.E., Coleman, R.E., et al.: Florbetapir (F18-AV-45) PET to assess amyloid burden in Alzheimer’s disease dementia, mild cognitive impairment, and normal aging. *Alzheimers Dement.* **9**(5 Suppl), S72–S83 (2013). <https://doi.org/10.1016/j.jalz.2012.10.007>
7. Marquié, M., Normandin, M.D., Vanderburg, C.R., Costantino, I.M., Bien, E.A., Rycyna, L.G., et al.: Validating novel tau positron emission tomography tracer [F-18]-AV-1451 (T807) on postmortem brain tissue. *Ann Neurol.* **78**(5), 787–800 (2015). <https://doi.org/10.1002/ana.24517>
8. Dosovitskiy, A., Beyer, L., Kolesnikov, A., Weissenborn, D., Zhai, X., Unterthiner, T., et al.: An Image is Worth 16x16 Words: Transformers for Image Recognition at Scale. In: International Conference on Learning Representations (ICLR) (2021). <https://doi.org/10.48550/arXiv.2010.11929>
9. Karypis, G., Kumar, V.: A Fast and High Quality Multilevel Scheme for Partitioning Irregular Graphs. *SIAM J. Sci. Comput.* **20**(1), 359–392 (1998). <https://doi.org/10.1137/S1064827595287997>
10. Petersen, R.C., Aisen, P.S., Beckett, L.A., et al.: Alzheimer’s Disease Neuroimaging Initiative (ADNI): clinical characterization. *Neurology* **74**(3), 201–209 (2010). <https://doi.org/10.1212/WNL.0b013e3181cb3e25>
11. Marcus, D.S., Fotenos, A.F., Csernansky, J.G., Morris, J.C., Buckner, R.L.: Open Access Series of Imaging Studies: Longitudinal MRI Data in Nondemented and Demented Older Adults. *J. Cogn. Neurosci.* **22**(12), 2677–2684 (2010). <https://doi.org/10.1162/jocn.2009.21407>
12. Albert, M.S., DeKosky, S.T., Dickson, D., et al.: The diagnosis of mild cognitive impairment due to Alzheimer’s disease: Recommendations from the National Institute on Aging–Alzheimer’s Association workgroups on diagnostic guidelines for Alzheimer’s disease. *Alzheimers Dement.* **7**(3), 270–279 (2011). <https://doi.org/10.1016/j.jalz.2011.03.008>

13. Bondi, M.W., Edmonds, E.C., Jak, A.J., et al.: Neuropsychological criteria for mild cognitive impairment improves diagnostic precision, biomarker associations, and progression rates. *J. Alzheimers Dis.* **42**(1), 275–289 (2014). <https://doi.org/10.3233/JAD-140276>
14. Nettiksimmons, J., DeCarli, C., Landau, S., Beckett, L., Alzheimer’s Disease Neuroimaging Initiative: Biological heterogeneity in ADNI amnesic mild cognitive impairment. *Alzheimers Dement.* **10**(5), 511–521.e1 (2014). <https://doi.org/10.1016/j.jalz.2013.09.003>
15. Gordon, B.A., McCullough, A., Mishra, S., et al.: Cross-sectional and longitudinal atrophy is preferentially associated with tau rather than amyloid β positron emission tomography pathology. *Alzheimers Dement (Amst)* **10**, 245–252 (2018). <https://doi.org/10.1016/j.dadm.2018.02.003>
16. Ossenkoppele, R., Smith, R., Ohlsson, T., et al.: Associations between tau, $A\beta$, and cortical thickness with cognition in Alzheimer disease. *Neurology* **92**(6), e601–e612 (2019). <https://doi.org/10.1212/WNL.0000000000006875>
17. Harrison, T.M., Du, R., Klencklen, G., Baker, S.L., Jagust, W.J.: Distinct effects of beta-amyloid and tau on cortical thickness in cognitively healthy older adults. *Alzheimers Dement.* **17**, 1085–1096 (2021). <https://doi.org/10.1002/alz.12249>
18. Lew, C.O., Zhou, L., et al.: MRI-based Deep Learning Assessment of Amyloid, Tau, and Neurodegeneration Biomarker Status across the Alzheimer Disease Spectrum. *Radiology.* 309(1), e222441 (2023). <https://doi.org/10.1148/radiol.222441>